

# Sulfur Transfer Melt Infiltration for High-Power Carbon Nanotube Sheets in Lithium-Sulfur Pouch Cells

Tom Boenke,<sup>[a, b]</sup> Paul Härtel,<sup>[a, b]</sup> Susanne Dörfler,<sup>\*[b]</sup> Thomas Abendroth,<sup>[b]</sup> Friedrich Schwotzer,<sup>[a]</sup> Holger Althues,<sup>[b]</sup> and Stefan Kaskel<sup>[a, b]</sup>

Among next-generation battery systems, the lithium-sulfur (Li–S) technology is attracting increasing attention driven by the low active material costs, high theoretical specific energy, and promising progress made in terms of its technology readiness level (TRL) in the recent years. However, the power density, especially in prototype cells, is an often neglected parameter being crucial for future application sectors. In this work, the cathode is redesigned by introducing a scalable, non-toxic, and homogeneous sulfur impregnation process for free-standing carbon scaffolds and tailorabile sulfur areal loading. This novel sulfur transfer melt infiltration is exemplarily applied to process carbon nanotube (CNT)-based Li–S cathode structures, but as a generic and scalable methodology is highly versatile. We demonstrate the development for CNT Buckypaper

(BP) and CNT powder-based dry transfer electrodes (DryFilm) as cathode host structures with the highly polysulfide (PS) solvating electrolyte system DME/DOL. In order to evaluate the practicability for high power application, the redesigned CNT BP cathode system with varying sulfur contents is employed in multi-layered pouch cell format with  $4 \mu\text{L mg}_\text{s}^{-1}$  for reduced electrolyte conditions. Additionally, first pouch cells with circular perforated aluminum current collector enable 80% weight savings of passive cathode material without compromising cell performance for free-standing thin-film cathodes. This study is an important step towards the development of lightweight Li–S cells for high power applications, such as drones or high altitude satellites.

## 1. Introduction

With the growing need for electrification across many application sectors, the development of new energy storage technologies is of increasing relevance.<sup>[1]</sup> A high specific energy of  $400 \text{ Wh kg}^{-1}$  and beyond, in combination with a certain power density are common requirements across all applications, such as large commercial vehicles, high altitude long endurance (HALE), high altitude pseudo satellites (HAPS), electric vertical take-off and landing (eVTOL) and electric passenger aircraft.<sup>[2,3]</sup> Higher energy battery systems will generally enable these vehicles to achieve extended range, longer mission duration, lighter vehicle weight or increased payload. Among the next-generation battery technologies, Li–S is attracting increasing attention driven by the significant advantages, e.g., the high theoretical specific capacity

( $1672 \text{ mAh g}^{-1}$ ) and low cost at large production volumes of sulfur as active material.<sup>[4,5]</sup> In combination with lithium metal, advanced prototype cells currently enable specific energy densities up to  $470 \text{ Wh kg}^{-1}$  at lab scale.<sup>[6]</sup> Still, commercialization has been limited by short cycle life and fast capacity fading mainly caused by parasitic side reactions between polysulfide species, the electrolyte and lithium metal anode, leading to dendritic growth and electrolyte consumption during cycling.<sup>[7,8]</sup> Especially the high current densities resulting from increased high areal capacities contribute to lithium anode and electrolyte degradation, and are consequently one factor for limiting the power density.<sup>[9,10]</sup> Enhancing the rate capability of Li–S batteries also accelerates iteration loops for the development of its components.<sup>[4]</sup> So far, only few values of power density or specific energies at C-rates  $>0.1 \text{ C}$  have been reported for Li–S prototype cells. Oxis Energy recently published  $300 \text{ Wh kg}^{-1}$  with maximum C-rate of  $3 \text{ C}$  and the Dalian University reported a pouch cell with  $350 \text{ Wh kg}^{-1}$  and  $60 \text{ W kg}^{-1}$ , that was cycled 30 times with  $0.2 \text{ C}$ .<sup>[11,12]</sup>

Similar to electrodes in state of the art Lithium ion batteries,<sup>[13]</sup> other factors affecting power density are e.g. electrode thickness, porosity, electrolyte amount or rather viscosity,<sup>[14–16]</sup> lithium transfer numbers,<sup>[17]</sup> lithium ion solvation,<sup>[18]</sup> mass/charge transfer<sup>[19]</sup> and the percolating network of the carbon material.<sup>[15,20]</sup> Based on the intrinsic insulating character of sulfur, carbonaceous materials are ideal candidates for a light-weight and conductive scaffold for electrochemical conversion (e. g. porous carbons fibers and carbon nanotubes).<sup>[21,22]</sup> Structural aspects such as specific surface area, pore size geometry and heteroatom doping are

[a] T. Boenke, P. Härtel, F. Schwotzer, Prof. Dr. S. Kaskel  
Department of Inorganic Chemistry I  
Technische Universität Dresden  
Bergstraße 66, 01069 Dresden, Germany

[b] T. Boenke, P. Härtel, Dr. S. Dörfler, Dr. T. Abendroth, Dr. H. Althues,  
Prof. Dr. S. Kaskel  
Department of Surface and Battery Technology  
Fraunhofer Institute for Material and Beam Technology (IWS)  
Winterbergstraße 28, 01277 Dresden, Germany  
E-mail: susanne.doerfler@iws.fraunhofer.de

 Supporting information for this article is available on the WWW under  
<https://doi.org/10.1002/batt.202100033>

 © 2021 The Authors. *Batteries & Supercaps* published by Wiley-VCH GmbH.  
This is an open access article under the terms of the Creative Commons Attribution License, which permits use, distribution and reproduction in any medium, provided the original work is properly cited.

key parameters for uniform sulfur and lithium sulfide utilization or rather precipitation.<sup>[23,24]</sup> Operando X-ray radiography revealed sulfur crystals on activated carbon fiber-based cathodes with a length of more than 1 mm in the highly polysulfide (PS) solvating electrolyte system DME/DOL.<sup>[25]</sup> The combination with SAXS analysis also showed that the precipitation of macroscopic sulfur and nanoscopic lithium sulfide crystals did not occur in the microporous structure as assumed, but on the outer surface of the carbon fiber.<sup>[26]</sup>

Carbon nanotubes (CNTs) with their tubular structure and high aspect ratio enable long electron pathways, high mechanical integrity, and low conductive percolation threshold.<sup>[27]</sup> The first free-standing CNT sheet was described as "Buckypaper" (BP) in 1998,<sup>[28]</sup> and its production has been further up-scaled ever since. Several publications have discussed the function of freestanding carbon structures in Li–S batteries as flexible, binder-free sulfur cathode scaffold, upper-current collector and interlayer between cathode and separator.<sup>[22,29,30]</sup> Vertically aligned VACNTs are also of particular interest providing long-axis orientation and rapid electrolyte penetration.<sup>[15,31]</sup> Free-standing electrodes with CNT as conductive additive have been discussed by a solvent-free dry film process due to a fibrillating PTFE binder system.<sup>[32]</sup> On a lab scale and for coin cell testing, various sulfur infiltration techniques for freestanding electrodes have been described: Melt infiltration, vapor deposition, liquid phase infiltration, spray coating, and electrochemical infiltration by polysulfide catholytes.<sup>[33]</sup> However, a scalable sulfur impregnation of freestanding carbon substrates with controllable areal loading for pouch cells has not been reported yet.

This study provides a strategy how to improve power density of Li–S prototype pouch cells by combining flexible, low-porosity CNT cathodes with varying but strictly controlled sulfur loading. Hereby, novel sulfur transfer melt infiltration enables the practical application of freestanding CNT electrodes with controlled sulfur mass distribution in Li–S prototype cells. The corresponding cathodes of CNT Buckypaper (BP) and CNT powder-based dry transfer electrode (DryFilm) were compared in regard of sulfur utilization and rate capability by employing a highly PS solvating electrolyte DME/DOL. For this purpose, results from coin cell measurements were analyzed at moderate electrolyte conditions ( $7 \mu\text{L mg}_5^{-1}$ ) and constant cathode design ( $2.0 \text{ mg cm}^{-2}$  sulfur mass loading, 50 wt-% sulfur,) for evaluation of the CNT structure-property relation. Subsequently, the most promising CNT BP results were transferred from coin cell to multi-layered pouch cells with reduced electrolyte conditions ( $4 \mu\text{L mg}_5^{-1}$ ). By varying the sulfur loading and sulfur content, important findings were gained that are crucial for the development of high power density Li–S cell designs. For the first time, the carbon cathode structure was combined with circular perforated aluminum current collector in order to realize 80% weight savings of passive cathode elements. Thin-film cathodes with low sulfur loadings can now exploit their advantages through higher sulfur utilization and rate capability in future cell development.

## 2. Results and Discussion

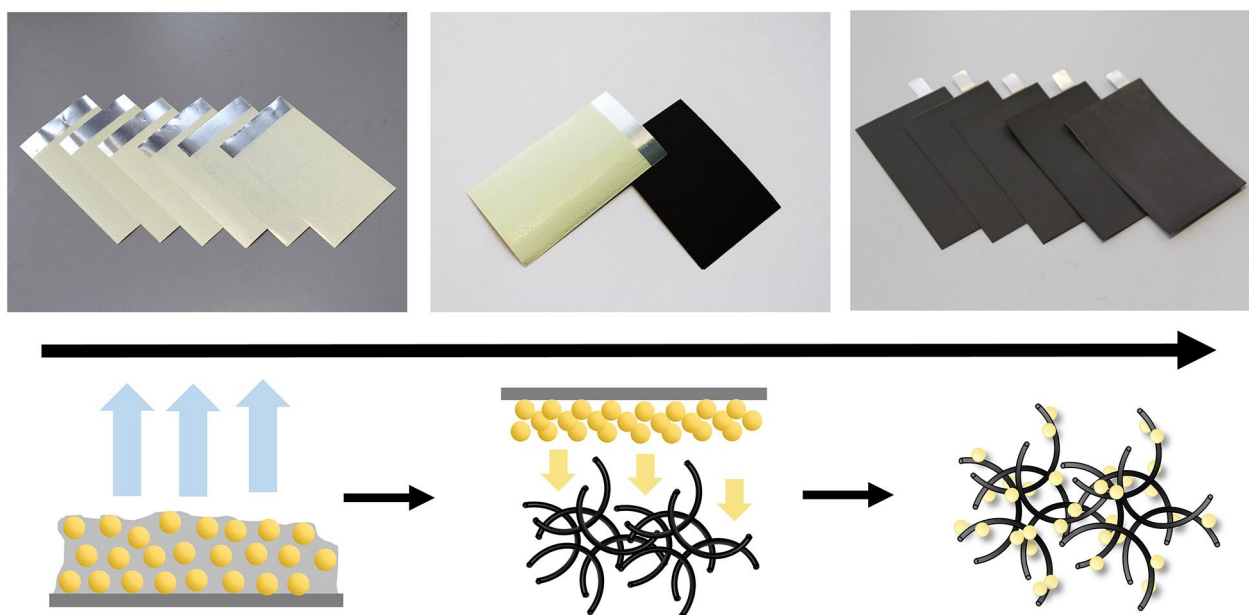
### 2.1. Sulfur Transfer Melt Infiltration

The sulfur transfer melt infiltration can be described as a scalable surface impregnation for free-standing, flexible electrodes due to a sulfur diffusion process from a sulfur transfer foil into a target carbon framework (Figure 1). This technique was developed for homogeneous sulfur distribution with linear correlation of wet film thickness and sulfur loading (see Figure S1a). In the first step, a well-dispersed sulfur slurry is used for a non-toxic casting process onto aluminum transfer foils. After drying for 10 min at  $80^\circ\text{C}$  solely sulfur remained on the transfer foil. For the second step, all sulfur sheets are stacked together with corresponding carbon electrodes ( $46 \times 71 \text{ mm}^2$ ) in a steel housing tool. The infiltration is carried out at  $155^\circ\text{C}$  and 1 h under argon atmosphere and enables homogeneous and complete sulfur diffusion with  $>99\%$  sulfur transfer yield, and the aluminum foil can be withdrawn afterwards. The final cathode design and cell assembly is implemented in step three. Up to 100 sheets can be infiltrated in one batch and the resulting freestanding sulfur cathodes are then ready for the implementation in pouch cells.

### 2.2. Carbon Nanotube Material Characterization

In the following, exemplarily two different types of CNT samples are compared regarding the carbon structure and electrochemical performance in Li–S batteries: A commercial, free-standing CNT Buckypaper (BP) and industrial multi-walled CNT (MWCNT) NC7000 for CNT powder-based dry transfer electrode (DryFilm).

TEM images of both pristine CNT materials are illustrated in Figure 2. The CNT BP is composed of CNT bundles with hierarchical diameter distribution between 10 nm to 150 nm, varying tube lengths and various numbers of carbon walls (Figure 2a, 2b). According to scientific nomenclature, tubular nanostructures are distinguished between carbon nanotubes (CNT) and carbon nanofibers (CNF).<sup>[27,34]</sup> Both structures can be produced via catalytic chemical vapor deposition (CCVD).<sup>[35,36]</sup> The concentric geometry of CNTs with diameters  $<100$  nm differs from vapor-grown CNFs (VGCNF) containing an entire hollow core based on linear filaments with more than 100 nm in diameter.<sup>[27]</sup> After optical evaluation, the majority of tubular structures can be attributed to multi-walled CNTs, and larger fibers probably correspond to VGCNF. Additionally, small spherical particles of 5 nm to 10 nm are located within tubular structures, which can be assigned to catalytic nanoparticles.<sup>[35]</sup> The CNT powder NC7000 consists of agglomerated MWCNT bundles with an homogenous outer diameter of 8–10 nm and inner diameter of 4–5 nm with wall thicknesses of 2–2.5 nm (Figure 2c, 2d). Based on the average interlayer spacing of 0.32–0.35 nm for CNTs, the industrial material NC7000 is composed of 5–8 carbon walls in tubular structure.<sup>[37]</sup> Summarizing, the pristine CNT materials vary in terms of tubular



### Step 1: Sulfur film casting    Step 2: Sulfur Transfer    Step 3: Cathode Design Melt Infiltration

**Figure 1.** Sulfur transfer melt infiltration consists of three-step process: sulfur film casting on aluminum transfer foils (step 1), sulfur transfer melt infiltration into carbon framework (step 2), and adaption of Li–S cathode design for cell assembly (step 3).

morphology, diameter, length and homogeneity in carbon composition.

The difference in CNT structures can also be confirmed via Raman spectroscopy (Figure 3a). Typical peaks for the corresponding D-mode (defective sites), G-mode (in-plane vibration of the C–C bond) and 2D-mode (second order vibration of D-mode) are observed with laser excitation wavelengths of  $\lambda_{\text{excitation}} = 514 \text{ nm}$  ( $1350 \text{ cm}^{-1}$ ,  $1584 \text{ cm}^{-1}$ ,  $2709 \text{ cm}^{-1}$ ) and  $\lambda_{\text{excitation}} = 785 \text{ nm}$  ( $1313 \text{ cm}^{-1}$ ,  $1585 \text{ cm}^{-1}$ ,  $2624 \text{ cm}^{-1}$ ) for both CNT BP and CNT NC7000.<sup>[38,39]</sup> The  $I_D/I_G$  ratios are calculated with mixed Gaussian-Lorentzian fittings between  $900 \text{ cm}^{-1}$  and  $2000 \text{ cm}^{-1}$  by determining peak areas of D-Band and G-Band. The characteristic values for  $\lambda_{\text{excitation}} = 514 \text{ nm}$  indicate a high amount of graphitic structures for CNT BP ( $I_D/I_G = 0.56$ ) and more defect sites for CNT NC7000 ( $I_D/I_G = 1.26$ ).<sup>[40]</sup> However, the interpretation of carbon purity can vary greatly by reason of heterogeneity within the CNT BP sample. Characteristic signals for the radial breathing mode (RBM) occur in low-frequency regions for CNT BP with  $\lambda_{\text{excitation}} = 785 \text{ nm}$  ( $120 \text{ cm}^{-1}$ ,  $178 \text{ cm}^{-1}$ ,  $275 \text{ cm}^{-1}$ ), similar as for CVD-grown CNTs with varying CNT diameters.<sup>[41]</sup> The origin is based on synchronous vibrations in radial direction of CNTs with small diameter such as single-walled CNTs and double-walled CNTs.<sup>[39,42]</sup> The RBM mode for CNT BP can be attributed to diameters lower 2.0 nm within tubular structure.<sup>[43]</sup>

The X-ray diffraction (XRD) patterns at  $2\theta$  of  $26.1^\circ$  (002),  $42.8^\circ$  (100),  $43.7^\circ$  (101), and  $53.8^\circ$  (404) reveal the typical inter-shell spacing of the concentric cylinders in graphitic carbon of CNT BP (Figure 3b). Most likely, the more filament-like CNTs with higher diameter and more graphitic layers provide more

lattice planes for diffraction. Ambiguous carbon patterns are observed between  $42^\circ$  and  $44^\circ$  for CNT NC7000. The signal at  $2\theta = 44.6^\circ$  in CNT BP can be related to different lattice planes of iron catalytic particles like Fe (400).<sup>[44]</sup>

Thermogravimetric analysis (TGA) under synthetic air for both CNT samples results in carbon purities of 93% (CNT BP) and 90% (CNT NC7000), as illustrated in Figure 3c. It should be noted that pyrolysis at higher temperatures leads to an oxidation of CNT catalyst metals to oxides with higher molecular weight and falsify the resulting ash weight.<sup>[27]</sup> The remaining ashes are analyzed additionally via XRD (Figure S2). The morphology of CNT BP ash appears as red flakes and can be identified as iron oxides.<sup>[45]</sup> Several diffraction signals can be assigned to  $\alpha\text{-Fe}_2\text{O}_3$ , e.g., at  $2\theta = 33.1^\circ$ ,  $35.6^\circ$ ,  $40.8^\circ$ ,  $49.4^\circ$ ,  $54.1^\circ$ ,  $62.4^\circ$  and  $64.0^\circ$  (Figure S2).<sup>[46]</sup> Depending on the pyrolysis temperature, different oxides can be formed, such as  $\text{Fe}_2\text{O}_3$  and  $\text{Fe}_3\text{O}_4$ .<sup>[47]</sup> Iron, cobalt, titanium, nickel, copper and combinations of these metals and/or their oxides widely used catalyst materials for CNT synthesis.<sup>[44,48,49]</sup> In contrast, the ash of NC7000 appears more greyish. Diffraction signals at  $2\theta = 35.7^\circ$ ,  $37.2^\circ$ ,  $43.5^\circ$ ,  $45.7^\circ$  and  $67.2^\circ$  could be attributed to characteristic signals of aluminum oxides, like  $\gamma\text{-Al}_2\text{O}_3$  and  $\text{Co}/\text{Al}_2\text{O}_3$  (Figure S2).<sup>[48]</sup>  $\text{Al}_x\text{O}_y$  material is applied as co-catalyst and/or catalyst support for various metals and promote the catalytic activity of CVD-based processes to increase the active surface.<sup>[50,51]</sup>

Energy dispersive X-ray mapping (EDX) provides further insight into the qualitative determination of catalysts in the resulting ash after TGA. As shown in Figure S3, the elements iron and oxygen are included for CNT BP, which matches well with XRD data. Elements for NC7000 with high intensity are

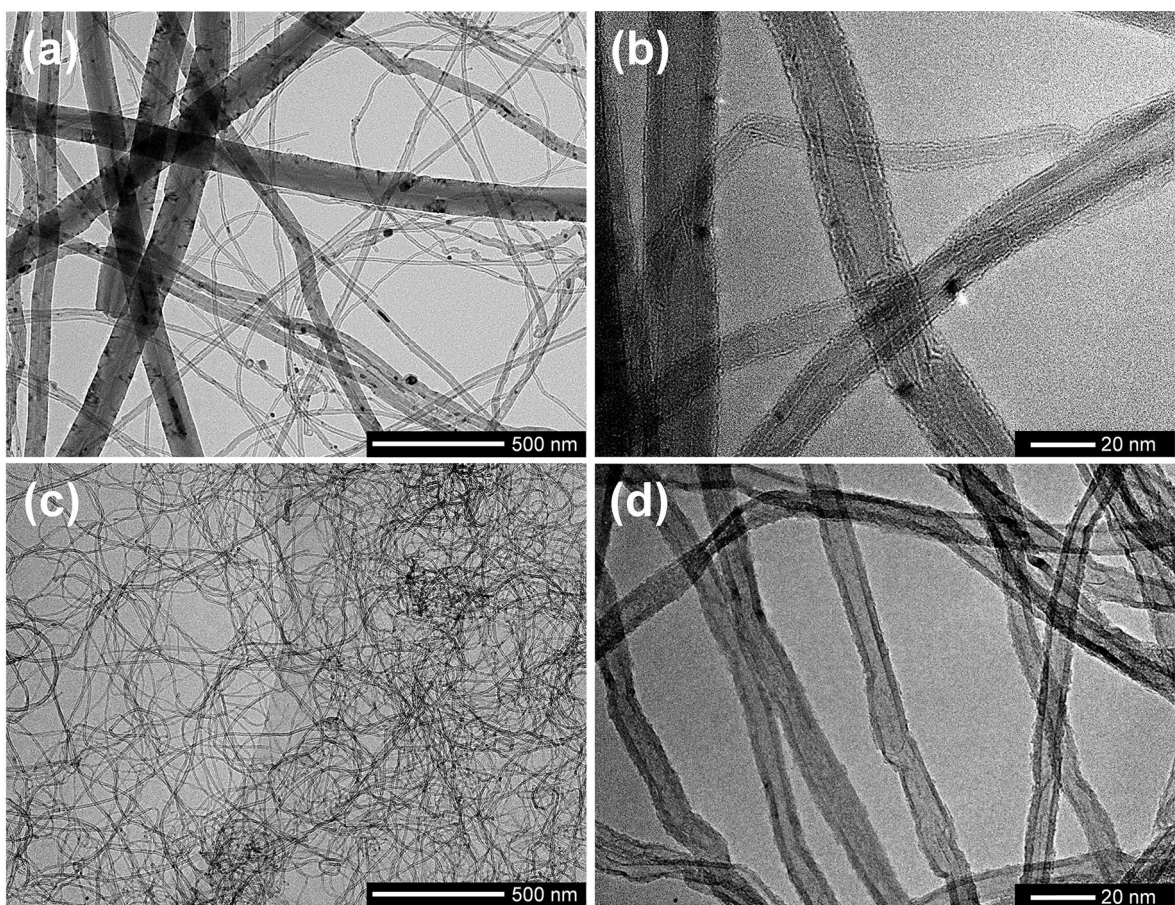


**Figure 2.** Transmission electron microscopy (TEM) with a magnification of 25,000x and 300,000x for pristine CNT BP (a, b) and CNT NC7000 (c, d).

aluminum and oxygen, and cobalt with low intensity. This may indicate the catalyst support of aluminum oxides for cobalt.<sup>[48,51]</sup>

Nitrogen physisorption isotherms of both materials correspond to reversible Typ II isotherms for nonporous or macroporous absorbents.<sup>[52]</sup> The pristine materials CNT BP and CNT NC7000 are characterized by  $38 \text{ m}^2 \text{ g}^{-1}$  and  $261 \text{ m}^2 \text{ g}^{-1}$  specific surface area ( $\text{SSA}_{\text{BET}}$ ),  $0.08 \text{ cm}^3 \text{ g}^{-1}$  and  $0.83 \text{ cm}^3 \text{ g}^{-1}$  total pore volume ( $p/p_0 = 0.97$ ), respectively (Figure 3d). These findings correspond well with other references<sup>[53]</sup> as well as with the TEM images: for the BP, a couple of filament-like carbon structures with remarkably thicker diameter can be observed that result in a lower specific surface area. The  $\text{SSA}_{\text{BET}}$  is considered as an average value in CNT BP.

Scanning electron microscopy (SEM) with magnification of 2,500x and 20,000x is carried out for scaffold structures of carbon electrodes (Figure 4). The CNT BP electrode consists of stacked CNT structures with hierarchical diameter distribution and high interspaces between the tubes. Smaller CNT filaments surround fiber structures with  $>10 \mu\text{m}$  length in disordered manner (Figure 4a, 4b). The morphology of the CNT Dryfilm electrode with NC7000 powder is uniform, and the entire structure appears to be more densified with local CNT agglomerations (Figure 4c, 4d). CNTs with thinner diameters prefer more cross-linking within the electrode, which significantly increases the proportion of conductive pathways and

may positively influence the electrochemical utilization of sulfur. In addition, an improved wetting behavior for liquid sulfur during melt infiltration at CNTs with small diameter could lead to a thinner and homogenous layer of sulfur crystals compared to thicker fiber structures.<sup>[22]</sup>

EDX measurements for CNT cathodes can be conducted after sulfur transfer melt infiltration, but the resolution of EDX mapping is intrinsically not high enough in order to reasonably analyze how homogeneously each single CNT is coated by sulfur. Thermal analysis of CNT BP cathodes (50%<sub>s</sub>) under argon atmosphere confirm 50% mass fraction of sulfur and 100% sulfur purity (see Figure S1b).

### 2.3. Electrochemical Characterization of CNT-Based Cathode Systems in Coin Cells vs. Li/Li<sup>+</sup>

In order to study the electrochemical performance of different CNT structures in Li–S cells, the cathode composition is kept constant with 50%<sub>s</sub> sulfur,  $2.0 \text{ mg}_s \text{ cm}^{-2}$  active material loading and  $0.5 \text{ g cm}^{-3}$  electrode density. Electrolyte amount is calculated for  $7.0 \mu\text{L mg}_s^{-1}$  ( $\sim 25 \mu\text{L}$ ). The standard electrolyte DME/DOL (1:1, v/v) is mixed with 1 M LiTFSI and 0.25 M LiNO<sub>3</sub>, containing ether solvents with high polysulfide (PS) solubility and lithium nitrate for a stable SEI formation and decreased PS

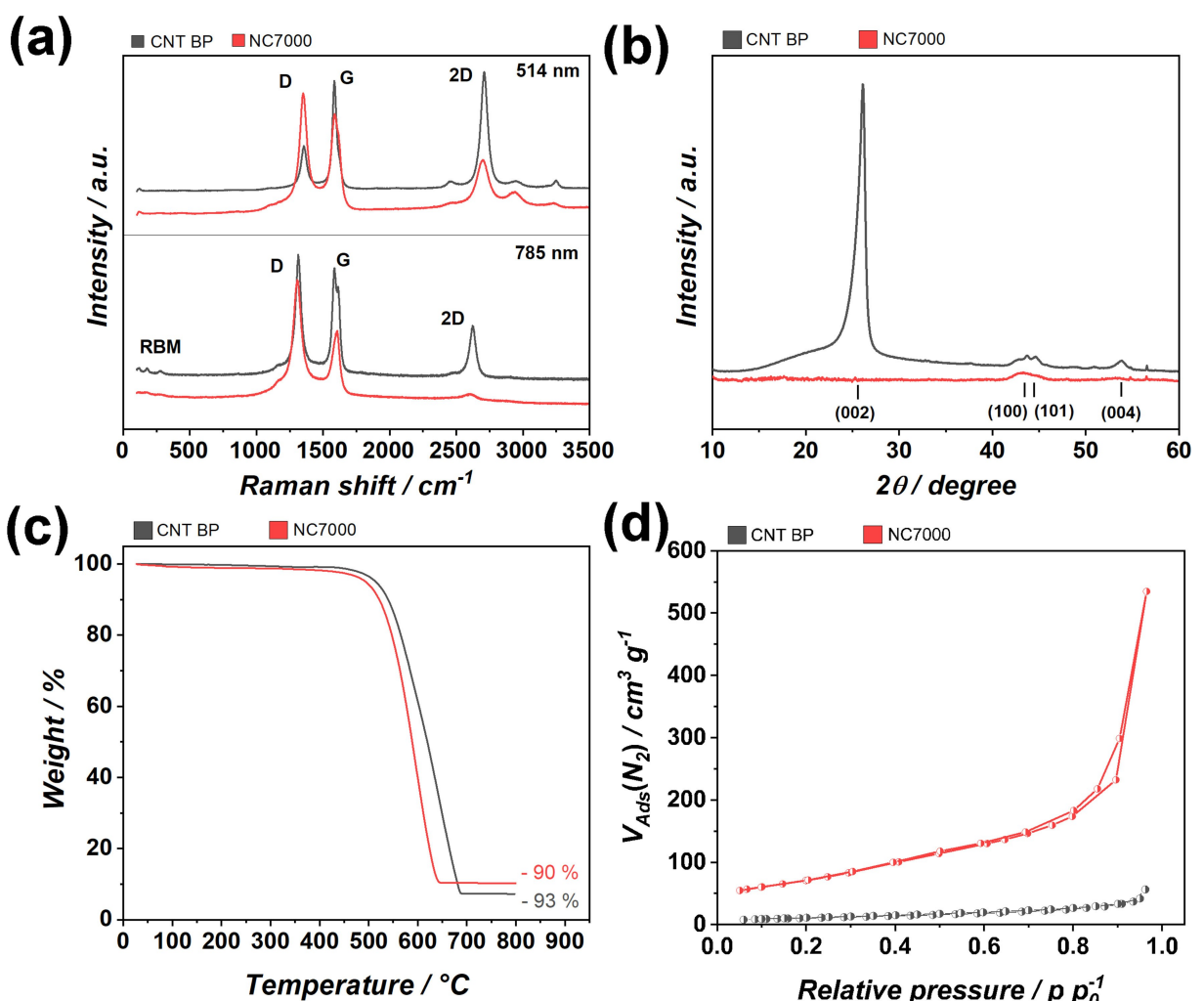


**Figure 3.** Material characterization with Raman analysis at 514 nm and 785 nm in comparison (a), X-ray powder diffraction (b), thermal analysis (c) and nitrogen physisorption (d) of CNT BP and CNT NC7000.

shuttle.<sup>[54,55]</sup> The electrochemical performance strongly depends on the electrolyte volume due to the dissolution of all reaction intermediates and a resulting increase in viscosity and internal cell resistance.<sup>[14,15,24]</sup> Herein, galvanostatic cycling tests are shown comparatively for both developed CNT cathodes in CR2016 coin cells (Figure 5a, Figure S4a,b).

For galvanostatic long-term stability testing at 0.1 C, the CNT BP cathode exhibits high initial discharge capacity (1208 mAh g<sub>s</sub><sup>-1</sup>) and low capacity retention within 100 cycles (782 mAh g<sub>s</sub><sup>-1</sup>) at. The Coulombic efficiency (CE) decreases slightly within 50 cycles from 98% to 94% and declines after 80 cycles to 60% due to enhanced PS shuttle (Figure 5a). In comparison, the cell with CNT DryFilm cathode achieves similar discharge capacity for the first cycle (1230 mAh g<sub>s</sub><sup>-1</sup>), stable CE values of 96% and lower capacity fading within 90 cycles (828 mAh g<sub>s</sub><sup>-1</sup>). The cell fails after 92 cycles caused by a short circuit or electrolyte dry-out. A possible reason for the short circuit in CNT DryFilm seems to be cell dry out due to electrolyte depletion and by anode corrosion, caused by higher discharge capacities and resulting in more stress during stripping and plating of lithium metal.<sup>[8]</sup> Both cathode systems

show similar voltage profiles in DME/DOL with characteristic first discharge plateau which is generated by the reduction of sulfur to long-chain PS species Li<sub>2</sub>Sn ( $8 \geq n \geq 4$ ) (Figure 5b). Differences in discharge capacities are caused by the conversion and precipitation of short-chain PS species (mainly lithium sulfide) during second discharge plateau at 2.12 V for CNT BP and 2.13 V for CNT DryFilm. During charging, two voltage plateaus at 2.23 V and 2.34 V can be observed for both CNT systems, indicating the oxidation of short-chain to long-chain PS and sulfur, respectively.<sup>[56]</sup> Regarding the electrochemical sulfur utilization, CNT DryFilm cathodes enable higher capacities for long-term and rate capability measurements. Different discharge C-rates are applied for rate capability testing: 0.05 C (0.17 mA cm<sup>-2</sup>), 0.1 C (0.33 mA cm<sup>-2</sup>), 0.2 C (0.67 mA cm<sup>-2</sup>), 0.5 C (1.67 mA cm<sup>-2</sup>), and 1 C (3.34 mA cm<sup>-2</sup>). The charge current at 0.1 C is not changed in order to minimize the degradation of lithium metal during plating.<sup>[10]</sup> The CNT BP achieves reasonable sulfur utilization at 0.05 C to 0.5 C by slightly increased overpotential (1257 mAh g<sub>s</sub><sup>-1</sup> to 878 mAh g<sub>s</sub><sup>-1</sup>), as shown in Figure 5d. The discharge capacity drastically drops at 1 C (239 mAh g<sub>s</sub><sup>-1</sup>). However, for CNT

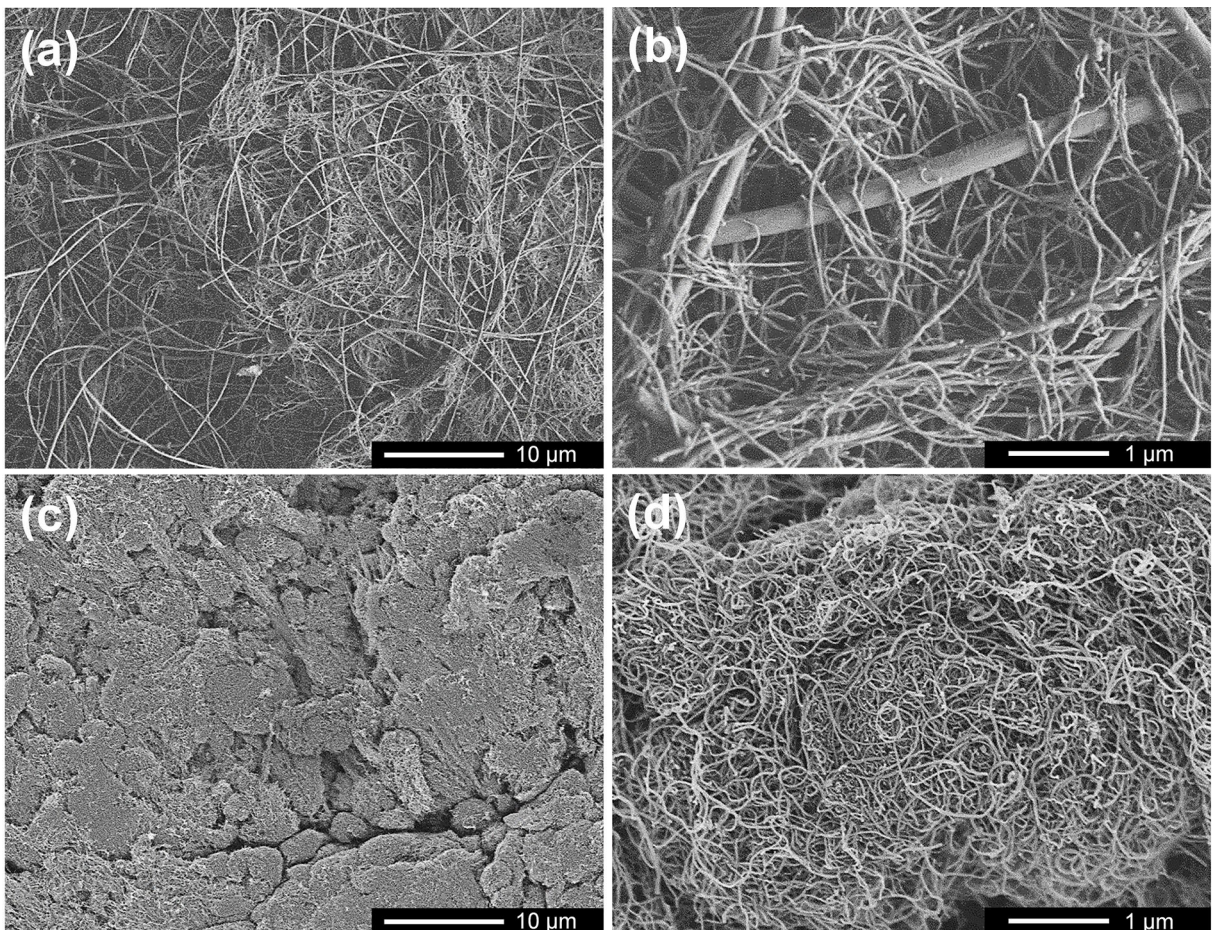


Figure 4. Scanning electron microscopy (SEM) with a magnification of 2.5x and 20,000x for the carbon electrodes CNT BP (a, b) and CNT DryFilm (c, d).

DryFilm cathodes a stable sulfur utilization is possible within the entire C-rate range from 0.05 C to 1 C (1288 mAh g<sup>-1</sup> to 985 mAh g<sup>-1</sup>). A remarkably high utilization of both voltage plateaus whilst slightly increased overpotential of the second plateau (2.1 V to 1.95 V) can be observed. Furthermore, this cathode consists of smaller MWCNT bundles with higher aspect ratio and enable increased redox kinetics on the carbon surface area and electron transport for PS reduction<sup>[22,30]</sup>. Both CNT cathode systems can regain the high capacity by decreased discharge currents. Principally, the DME/DOL electrolyte has a relatively high ionic conductivity, but due to the high PS solubility and the cluster formation of short-chain PSs, small amounts of electrolyte lead to an increase in viscosity and thus increased polarization, which reduce the utilization of active material.<sup>[3,19,55,57]</sup>.

Further investigations regarding redox mechanism are done by cyclic voltammetry (CV) with constant scan rate of 0.01 mVs<sup>-1</sup> between 2.6 V and 1.8 V (Figure 5c, Figure S2c,d). Typical reduction peaks during cathodic scan for both systems at 2.30 V/2.06 V (CNT BP) and 2.31 V/2.03 V (CNT DryFilm) are observed and correspond to the transformation of long-chain and short-chain PS species Li<sub>2</sub>S<sub>n</sub> ( $8 \geq n \geq 4$ ) and Li<sub>2</sub>S/Li<sub>2</sub>S<sub>2</sub>, respectively.<sup>[58]</sup> The two-step reduction process is revealed in the galvanostatic two-plateau discharge curve. During charg-

ing, two overlapping anodic peaks are observed at 2.28 V/2.30 V for CNT-BP and 2.31 V/2.39 V for CNT-DryFilm, indicating the oxidation of lithium sulfide to sulfur. In contrast, only slight differences are observed in terms of peak shape and voltage shift between both cathode systems. These results imply a similar redox mechanism for DME/DOL under moderately electrolyte conditions and low scan rate.

As already reported, the amount of electrolyte has a tremendous impact on cell chemistry, so the results should be cautiously discussed.<sup>[55]</sup> Nevertheless, the moderate electrolyte amount (7 μL mg<sup>-1</sup>) in CR2016 coin cells cannot represent practical aspects, not even under lean electrolyte conditions as pressure distribution and dead volume differs from practical pouch cells.<sup>[59]</sup>

#### 2.4. CNT Buckypaper Pouch Cell Development and Electrochemical Characterization vs. Li/Li<sup>+</sup>

Prior cathode preparation, CNT BP electrodes are cut into the final cathode design of 46 × 71 mm<sup>2</sup> (Figure 6a). For pouch cell development, three double-sided cathodes of CNT BP are used for electrochemical investigation as a first feasibility study under moderate electrolyte conditions (4 μL mg<sup>-1</sup>). Buckypaper

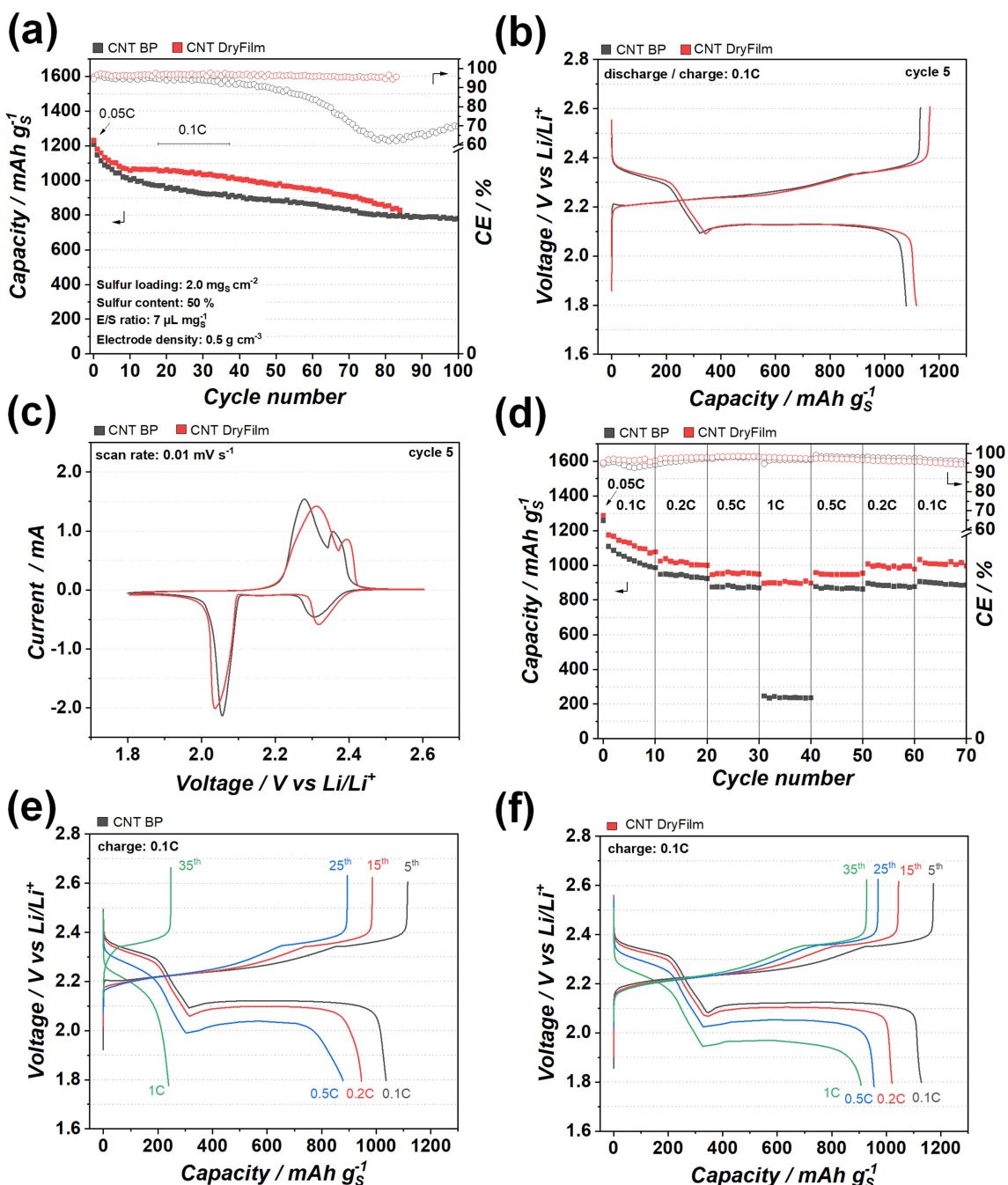


**Figure 5.** Galvanostatic cycling results and voltage profiles in DME/DOL of CNT BP (black) and CNT DryFilm (red) cathodes in CR2016 coin cells are shown for long term testing at 0.1 C (a–b). Cyclic voltammetry is carried out with 0.01 mV s<sup>-1</sup> scan rate and constant cathode composition of CNT BP (black) and CNT DryFilm (red) (c) and rate capability measurements at 0.05 C to 1 C (e–f). All cathodes contain 50% sulfur, 2.0 mg<sub>S</sub> cm<sup>-2</sup> active material loading, 0.5 g cm<sup>-3</sup> electrode density and 7 µL mg<sub>S</sub><sup>-1</sup> electrolyte.

is chosen as it leads to a free-standing CNT/sulfur composite and can be laminated on an aluminum current collector, as shown in Figure 6b. Hereby, varying CNT BP loadings (2.0, 1.5 and 1.0 mg<sub>BP</sub> cm<sup>-2</sup>) are infiltrated with 50 wt-%<sub>S</sub> sulfur for equal sulfur loadings (2.0, 1.5 and 1.0 mg<sub>S</sub> cm<sup>-2</sup>). In addition, cathodes with 33%<sub>S</sub> sulfur and 1.0 mg<sub>S</sub> cm<sup>-2</sup> combined with 2.0 mg<sub>BP</sub> cm<sup>-2</sup> are manufactured equally. The aim was to investigate the C-rate stability and the impact of charge/mass transfer with varying amounts and ratios of sulfur in cathodes

structures, similar as in former studies reported by Brückner et al. at coin cell level.<sup>[15]</sup>

As illustrated in Figure 7, four different sulfur cathode variations are tested in pouch cells under galvanostatic rate capability testing conditions as discussed for coin cells beforehand based on the specific capacity of sulfur (1672 mAh g<sup>-1</sup>). In terms of sulfur utilization, all discharge capacities increase both with lower sulfur loading and sulfur content which matches well with the research findings gained with VA-CNTs<sup>[15]</sup>. The

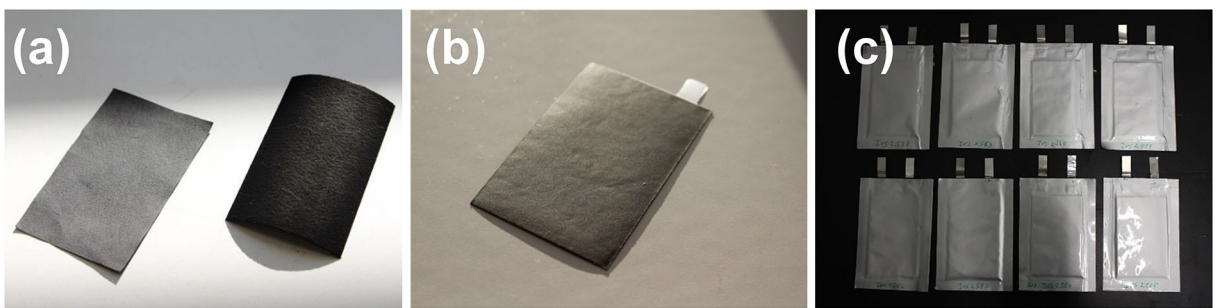


**Figure 6.** Pristine carbon electrodes of CNT BP (a, left) and CNT DryFilm (a, right), sulfur infiltrated CNT BP cathode in pouch cell design (b) and multi-layered pouch cells (c).

differences are less pronounced at low current rates (0.1 C), but highly differ at high current rates (1 C). All cathode systems presented herein can recover the discharge capacities after the rate capability testing.

The sulfur utilization of the CNT BP pouch cell with 50 wt-%<sub>S</sub> sulfur and 2.0 mg<sub>S</sub> cm<sup>-2</sup> active material (4 μL mg<sub>S</sub><sup>-1</sup>) can be directly compared to the CNT BP coin cell measurements (7 μL mg<sub>S</sub><sup>-1</sup>) (Figure 7a). The initial capacities at 0.05 C (1209 mAh g<sub>S</sub><sup>-1</sup>) and 0.1 C (1058 mAh g<sub>S</sub><sup>-1</sup>) are approximately comparable, but the pouch cell shows inferior C-rate performance at 0.2 C (892 mAh g<sub>S</sub><sup>-1</sup>), 0.5 C (637 mAh g<sub>S</sub><sup>-1</sup>) and 1 C (204 mAh g<sub>S</sub><sup>-1</sup>) caused by higher electrolyte viscosity and strengthened internal resistance at reduced electrolyte volumes in pouch cells. By increasing the current rate, especially the second plateau is shortened due to the mass transfer resistance, as reported by Zhang et al.<sup>[19]</sup> At peak current of 1 C only 200 mAh g<sub>S</sub><sup>-1</sup> is achieved within the first discharge plateau up to 1.8 V, which corresponds to the reduction of long-chain PS species. The sulfur utilizations by reducing the sulfur mass loading with constant 50%<sub>S</sub> active material raises step-wise between 2.0 and 1.0 mg<sub>S</sub> cm<sup>-2</sup>. In particular, the capacity collapse at 1 C is suppressed, increased voltage plateaus and discharge capacities of 565 mAh g<sub>S</sub><sup>-1</sup> with 1.5 mg<sub>S</sub> cm<sup>-2</sup> (50%<sub>S</sub>) and 950 mAh g<sub>S</sub><sup>-1</sup> with 1.0 mg<sub>S</sub> cm<sup>-2</sup> (50%<sub>S</sub>) are still reachable (Figure 7b, 7c). A remarkably increase of discharge with 33 wt-%<sub>S</sub> sulfur by maintaining 1.0 mg<sub>S</sub> cm<sup>-2</sup> sulfur loading is observed with between 0.05 C and 1 C with 1415 mAh g<sub>S</sub><sup>-1</sup> to 1116 mAh g<sub>S</sub><sup>-1</sup>, respectively (Figure 7d). In this case, all voltage curves at each current rate indicate the conversion of sulfur to short-chain reaction product. and the overpotential for the second plateau is slightly reduced up to 1 C. The average cell voltages for all cells are shown in Table S1. At lower rates we observe a second sub-plateau between 2.1 V and 2.0 V for the second discharge plateau in the first cycle. This phenomenon has been mentioned before without any further discussion and might need future investigation.<sup>[60]</sup> We suspect an electro-catalytic effect of the CNT structure and remaining PS species on the chemical conversion to lithium sulfides.<sup>[26]</sup>

The increase in capacity by lowering the sulfur loading whilst maintaining constant sulfur content can be explained by reduced internal cell resistance, which is caused by the reduction mass and charge transfer resistance between conductive carbon matrix and insulating active material<sup>[19,61]</sup>. When

the mass portion of active material in the cathode is reduced, more active surface of the carbon structure is provided for the conversion of sulfur and PS species, respectively. In summary, sulfur utilization can be significantly improved, especially at higher current rates at same electrolyte volumes of 4 μL mg<sub>S</sub><sup>-1</sup>. At lower current rates, the influence of sulfur loading can be neglected as the kinetic hindrance loses influence. The corresponding discharge capacities are illustrated in Figure 7e. All pouch cells exhibit the recovery of discharge capacities within lower C-rates after the peak current at 1 C. During cycling, stable CEs between 97% to 99% additionally confirm less side reactions on lithium anode side. This can be explained by the decreased current densities due to the lower sulfur contents, which lead to a less stress and decreased lithium dendrite formation for lithium metal.<sup>[10]</sup>

The calculation for the specific energy densities are based on the first pouch cell results with three double-sided cathodes and 4 μL mg<sub>S</sub><sup>-1</sup> DME/DOL electrolyte and 50 μm lithium foil for each cathode side without any cell packaging and tabs (Figure 7f and Table S1). The highest specific energy is determined with 273 Wh kg<sup>-1</sup> for the non-optimized pouch cell with 2.0 mg<sub>S</sub> cm<sup>-2</sup> sulfur loading (0.655 Ah, 50 wt-%<sub>S</sub>) at low current of 0.05 C (Figure 7f, black). The capacity loss and reduction of cell voltage due to increased currents result in a constant energy loss up to 247 Wh kg<sup>-1</sup> (0.1 C), 203 Wh kg<sup>-1</sup> (0.2 C), 140 Wh kg<sup>-1</sup> (0.5 C) and 50 Wh kg<sup>-1</sup> (1 C), therefore only 18% specific energy finally remain.

The pouch cell with 1.5 mg<sub>S</sub> cm<sup>-2</sup> sulfur loading (0.491 Ah, 50 wt-%<sub>S</sub>) exhibits comparable results up to 0.2 C, but shows a lower decrease for higher currents at 1 C with 99 Wh kg<sup>-1</sup> (Figure 7f, red). Cathode compositions with lowered sulfur loadings of 1.0 mg<sub>S</sub> cm<sup>-2</sup> (0.328 Ah, 50%<sub>S</sub> and 33%<sub>S</sub> sulfur) achieve higher sulfur discharge capacities but can only provide 234 Wh kg<sup>-1</sup> and 230 Wh kg<sup>-1</sup> at 0.05 C due to the lowered areal capacity and higher proportion of passive elements like current collector foil (Figure 7f, blue/green). Furthermore, the reduced amount of active material enables good rate capabilities up to 1 C with comparatively high values of 159 Wh kg<sup>-1</sup> and 177 Wh kg<sup>-1</sup>, respectively. In this case, 68% and 77% of the specific energy with thin-film cathodes are still available. This contrary trend of the specific energy for pouch cells with varying sulfur loading should be fundamentally observed for

## Pouch cells with full area aluminum current collector

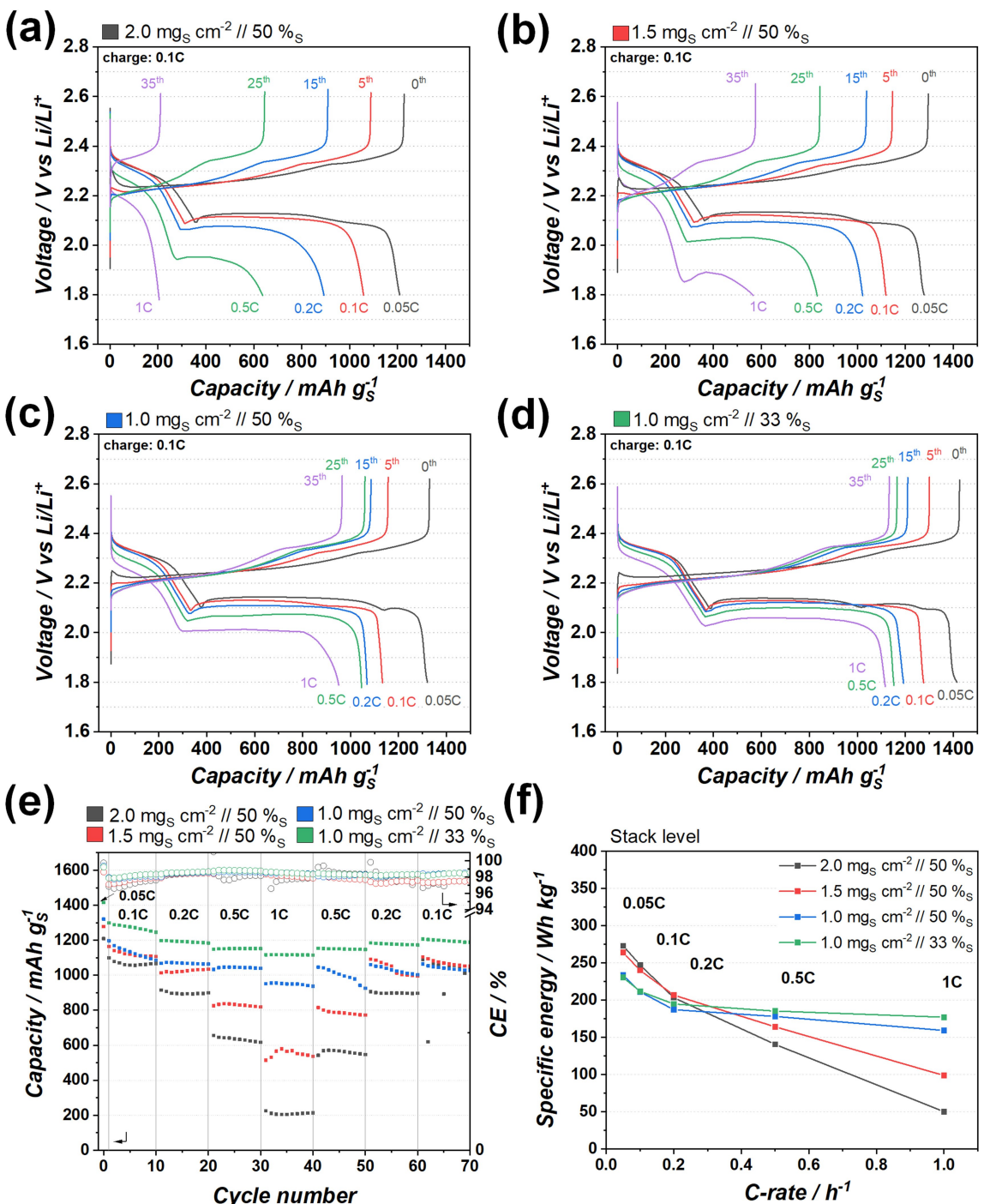


**Figure 7.** Discharge and charge slopes derive from rate capability measurements of multi-layered CNT BP pouch cells with full area aluminum current collector. The electrochemical performance between 0.05 C and 1 C (cycle 0, 5, 15, 25 and 35) is illustrated for cathode compositions with 2.0 mg<sub>S</sub> cm<sup>-2</sup> (50%), (a, black), 1.5 mg<sub>S</sub> cm<sup>-2</sup> (50%<sub>S</sub>) (b, red) and 1.0 mg<sub>S</sub> cm<sup>-2</sup> (50%<sub>S</sub>) (c, blue), 1.0 mg<sub>S</sub> cm<sup>-2</sup> (33%<sub>S</sub>) (d, green). The electrolyte amount is set to 4 μL mg<sub>S</sub><sup>-1</sup> of DME/DOL. Discharge capacities for the entire experiment are shown comparatively for 70 cycles (e). The specific energy on stack level without tabs and packaging is calculated as a function of current densities for all CNT/sulfur compositions with 4 μL mg<sub>S</sub><sup>-1</sup> of DME/DOL (f).

next cell developments. Still, the excess of electrolyte and lithium metal at lower sulfur loadings has to be discussed.

### 2.5. Perforated Aluminum Current Collector

In order to compensate for the unfavorable active to inactive mass ratio of thin-film cathodes (<1.5 mg<sub>S</sub> cm<sup>-2</sup>), we introduce

the circular perforation of the aluminum current collector in combination with free-standing cathode structures (Figure 8). Hereby, 80% weight reduction with 9.5 mm circular recesses enable increased gravimetric energy densities. First, the electrochemical performance was comparatively evaluated under same conditions as the non-perforated current collector. Pouch cell assembly with varying sulfur cathode compositions are produced equally to full area current collector pouch cell concepts. Due to the perforation the electrolyte volume was set to  $4.5 \mu\text{L mg}_{\text{s}}^{-1}$ , respectively. All experimental data concluding discharge and charge slopes, discharge capacities and calculated specific energy density on stack level are summarized in Figure 9 and Table S2.

As mentioned before, the electrolyte volume is the most important factor regarding gravimetric energy density and electrochemical conversion of Li–S cell.<sup>[59]</sup> A direct comparison is not possible as the electrolyte quantities differ for both cells due to the minimum volume of the pouch cells that need to be filled out. When employing the perforated current collector in a pouch cell with only three double-sides cathodes, a bit more electrolyte volume needs to be implemented. Nevertheless, conclusions can be drawn within the series of measurements. An increase in the discharge capacities with respect to lower sulfur loadings and higher currents up to 1 C are similar to the pouch cell result generated with the non-perforated current collector. The rate capability over 70 cycles differs only slightly from the full area current collector system (Figure 9). The sulfur loadings with  $2.0 \text{ mg}_{\text{s}} \text{ cm}^{-2}$  and  $1.5 \text{ mg}_{\text{s}} \text{ cm}^{-2}$  (50%<sub>s</sub>) still suffer from poor rate capability for 1 C despite high initial discharge capacities of  $1299 \text{ mAh g}_{\text{s}}^{-1}$  and  $1299 \text{ mAh g}_{\text{s}}^{-1}$  (0.05 C), respectively. Especially the gap between 1 C and 0.5 C (Figure 9a, 9b) should be investigated. Average cell voltage and cycling parameters are compared in Table S2. As for the full areal current collector, the cathode composites with only  $1.0 \text{ mg}_{\text{s}} \text{ cm}^{-2}$  also enable high capacities up to 1 C of  $1322 \text{ mAh g}^{-1}$  and  $1442 \text{ mAh g}^{-1}$  (50%<sub>s</sub> and 33%<sub>s</sub>) with  $4.5 \mu\text{L mg}_{\text{s}}^{-1}$  electrolyte.

It is important to mention that using the same sulfur content of 50%<sub>s</sub>, the capacity at lower currents of 0.1 C and reduced electrolyte volume only slightly differ and a trend only becomes apparent at higher current rates (Figure 9e). In a

direct comparison between the cell systems with different current collectors, no remarkable difference is observed for discharge capacity, cycle stability and average cell voltage. The impact of the perforation process (80% weight loss) is neglectable for the electrochemical performance at low sulfur loadings and thin cathode systems. These data also have to be converted to stack level in terms of their specific energy. (Figure 9f and Table S2). The calculation is based on an electrolyte amount of  $4.5 \mu\text{L mg}_{\text{s}}^{-1}$ , which impacts the energy density tremendously due to the high gravimetric proportion and the lithium anode ( $50 \mu\text{m}$ ) is still oversized based on the nominal capacity of lithium (297% and 615% for  $2.0$  and  $1.0 \text{ mg}_{\text{s}} \text{ cm}^{-2}$ ). Also for the perforated current collector, an indirect proportional effect with respect to sulfur loading and C-rate capability is observed. The specific energy at lower currents decreases with thinner cathodes and lower sulfur contents. Nevertheless, the highest specific energy density (stack level) at 1 C reaches up to  $179 \text{ Wh kg}^{-1}$  and  $189 \text{ Wh kg}^{-1}$  with thin cathode compositions of  $1 \text{ mg}_{\text{s}} \text{ cm}^{-2}$  (50 wt-%<sub>s</sub> and 33 wt-%<sub>s</sub>). Also for this system including a perforated current collector, so-called “projected” energy densities are extrapolated. This calculation include 40 double-sided CNT BP cathodes, thin lithium metal anodes ( $50 \mu\text{m}$ ), and weight savings of inactive material by varying perforation concepts for the free-standing CNT cathodes. Depending on the application and its energy and power requirements, thin-film cathodes with lower sulfur loadings than  $1.5 \text{ mg}_{\text{s}} \text{ cm}^{-2}$  are ideal candidates for cycling at higher C-rates in combination with mass reduction due to the perforation leading to specific energy densities of  $300 \text{ Wh kg}^{-1}$ .<sup>[11]</sup> Otherwise, high capacity cathode systems with sulfur loadings  $> 2.0 \text{ mg}_{\text{s}} \text{ cm}^{-2}$  for free-standing electrode concepts achieve gravimetric energy densities up to  $> 400 \text{ Wh kg}^{-1}$ .<sup>[59]</sup>

### 3. Conclusions

A redesign of sulfur/carbon cathodes was carried out in order to potentially improve the power density of Li–S prototype cells. A scalable method for the homogeneous transfer infiltration of sulfur with controllable areal loading was developed for two different CNT cathode structures: free-standing CNT Buckypaper (BP) and CNT powder-based dry transfer electrodes (DryFilm). The electrochemical performance of CNT cathodes was evaluated in state-of-the-art electrolyte DME/DOL on coin cell level and could be transferred into multi-layered pouch cells with reduced electrolyte amounts of  $4 \mu\text{L mg}_{\text{s}}^{-1}$ . It turned out that the CNT BP composite was the most promising concept to test in pouch cells as these electrodes are free-standing and available in low carbon loadings. Hence, pouch cells with varying sulfur loading and content were built and evaluated regarding the rate capability. In conclusion, the lower the sulfur areal loading and mass portion in the cathode, the higher the rate capability of the pouch cell. However, with higher sulfur areal loading and mass portion in the cathode the specific energy increases. Furthermore, the circular perforation of aluminum current collector

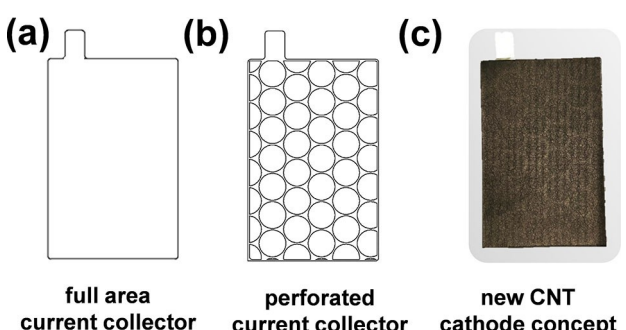


**Figure 8.** Aluminum current collector concepts are illustrated comparatively for full area (a) and circular perforated concepts (b). The cathode redesign combines CNT BP scaffold structure and the aluminum perforation concept for 80% weight loss of inactive material (c).

## Pouch cells with perforated aluminum current collector

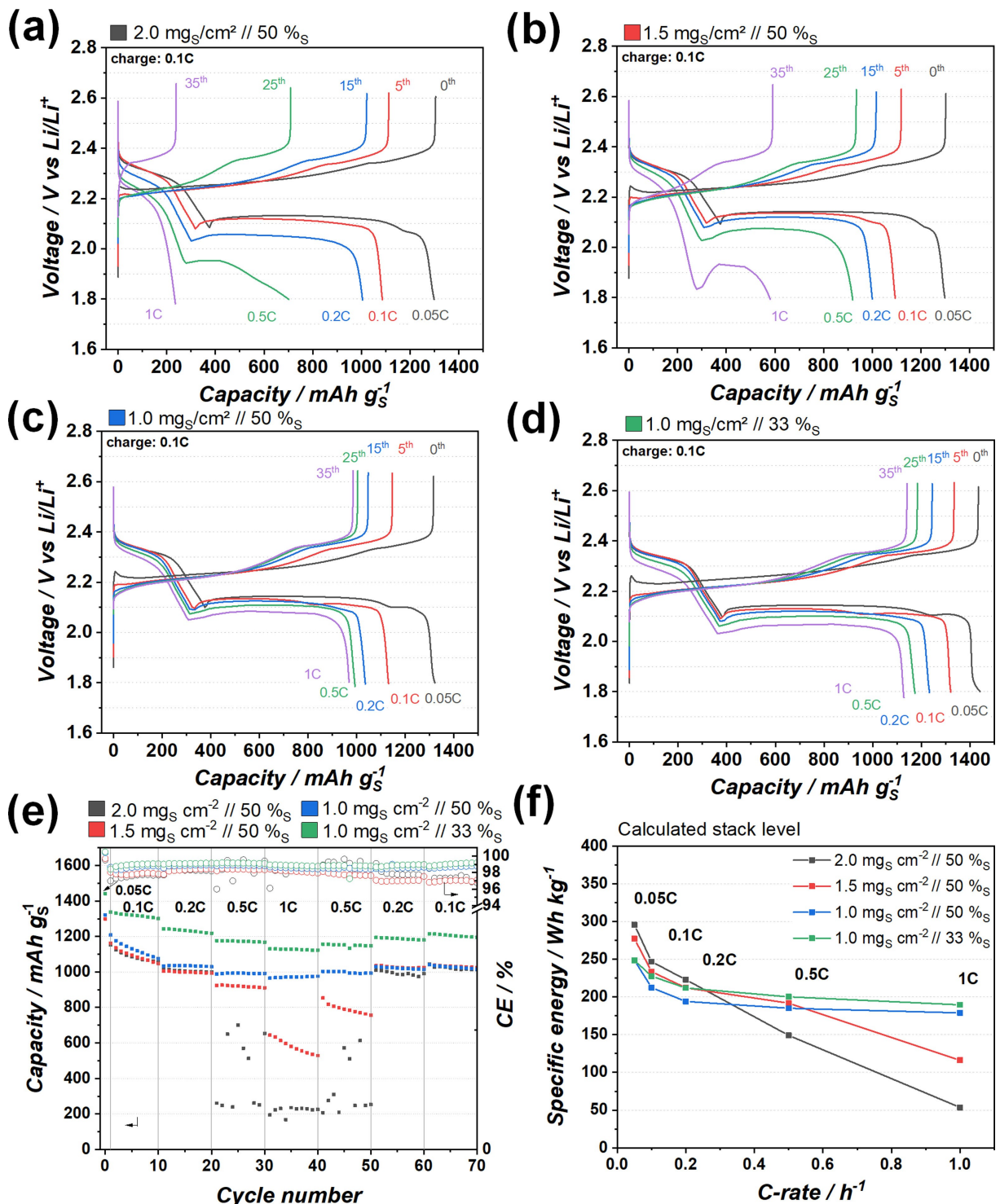


**Figure 9.** Discharge and charge slopes derive from rate capability measurements of multi-layered CNT BP pouch cells with circular perforated aluminum current collector. The electrochemical performance between 0.05 C and 1 C (cycle 0, 5, 15, 25 and 35) is illustrated for cathode compositions with  $2.0 \text{ mg}_{\text{S}} \text{ cm}^{-2}$  (50%) (a, black),  $1.5 \text{ mg}_{\text{S}} \text{ cm}^{-2}$  (50%) (b, red),  $1.0 \text{ mg}_{\text{S}} \text{ cm}^{-2}$  (50%) (c, blue) and  $1.0 \text{ mg}_{\text{S}} \text{ cm}^{-2}$  (33%) (d, green). The electrolyte amount is set to  $4.5 \mu\text{L} \text{ mg}_{\text{S}}^{-1}$  of DME/DOL. Discharge capacities for the entire experiment are shown comparatively for 70 cycles (e). The specific energy on stack level without tabs and packaging is calculated as a function of current densities for all CNT/sulfur compositions with  $4.5 \mu\text{L} \text{ mg}_{\text{S}}^{-1}$  of DME/DOL (f).

with 80% weight loss of inactive cathode material was investigated comparatively in multi-layered pouch cells, as well.

The direct comparison of full area and perforated current collector concepts regarding the electrochemical performance

does not show any decisive impact. Therefore, the combination of thin-film cathodes with lower sulfur loadings with the adaption or absence of aluminum current collector concepts can be attractive candidates for high power and energy cells. These findings are important to develop pouch cells for future applications. In addition, this strategy can shorten iterative loops for the holistic development of Li–S prototype cells.

## Experimental Section

### Material characterization

The carbon morphology is characterized by scanning electron microscopy (SEM) in a Hitachi SU8020 (2.0 kV acceleration voltage) and transmission electron microscopy (TEM) in a JEOL JEM 1400 (12.0 kV acceleration voltage). Further investigations of pyrolytic ash is conducted by energy dispersive X-ray spectroscopy (EDX) with a JEOL-JSM-6610. This technique exhibit the qualitative evaluation of elemental composition of ash products after pyrolysis under synthetic air. Thermal analysis is performed by a Netzsch STA 409 PC LUXX under argon and synthetic air with a heating rate of  $5\text{ K min}^{-1}$ . Nitrogen physisorption measurements are performed at 77 K on a NOVA 4000e after degassing the samples under vacuum for 12 h at 150 °C. The specific surface area is calculated based on multi-point Brunauer–Emmett–Teller (BET) method in the range of relative pressure  $p/p_0 = 0.05\text{--}0.25$  and the total pore volume is determined at  $p/p_0 = 0.97$ . Raman spectroscopy is carried out with a Renishaw inVia spectrometer using 514 nm and 785 nm excitation laser wavelength. Data analysis is realized with mixed Lorentz–Gauss peak fitting between 900 cm<sup>-1</sup> and 2000 cm<sup>-1</sup> by determining the corresponding peak area ratios of D-band and G-band ( $I_D/I_G$ ). X-ray diffraction (XRD) expose cristallinity of carbon material and the corresponding ashes by using a D5005 XRD system (Siemens) at room temperature (CuK $\alpha$ , 40 kV, 40 mA). CNT samples are placed in top of a circular silicon wafer, and the ash still requires adhesive tape for fixation.

### Carbon electrode preparation

Carbon nanotube (CNT) electrodes are separately prepared prior to sulfur impregnation. Commercial freestanding CNT Buckypaper (BP) (MWNT Buckypaper, NTL) are used without any further treatments. For comparison, flexible CNT powder-based dry transfer electrodes (Dry Film) are produced by shearing forces by a continuous roll-to-roll laminating process (DRYtraec®, Fraunhofer IWS) onto primer coated aluminum foil (20  $\mu\text{m}$ , MTI). The CNT DryFilm electrode is made of industrial multi-walled CNTs (NC7000, 90% purity, Nanocyl) and polytetrafluoroethylene (PTFE) binder in a 95/5 weight ratio. Both carbon electrode concepts are cut to the final pouch cell electrode dimension (71  $\times$  46 mm<sup>2</sup>).

### Sulfur transfer melt infiltration

In the first step, sulfur powder (precipitated, Alfa Aesar, >99.5%) is mixed together with a non-toxic volatile surfactant in a ball mill for 10 min to a viscous sulfur suspension (30 wt-% sulfur). The paste is coated by doctor blade technique on tailored aluminum transfer foils (20  $\mu\text{m}$ , MTI) in size of the pouch cell electrode dimension (71  $\times$  46 mm<sup>2</sup>). The specific sulfur loading is controlled by blade casting with the corresponding wet film thickness (100  $\mu\text{m}$   $\sim$  2.0 mg<sub>s</sub> cm<sup>-2</sup>). All sheets dry for 10 min at 80 °C and overnight at room temperature. In the second step, all carbon-based electrodes are placed on top of sulfur foils in a steel housing cask (Fraunhofer

IWS). The sulfur transfer melt infiltration is carried out at 155 °C for 1 h under Argon atmosphere. The aluminum transfer foil is removed afterwards.

### Sulfur cathode preparation for coin cells

The sulfur impregnation of carbon electrodes is ensured by the sulfur transfer melt infiltration at 155 °C for 1 h under argon. Final sulfur loadings are determined by weight before and after infiltration. The cathode composition for coin cell testing is set to  $50 \pm 1$  wt-%<sub>s</sub> sulfur,  $2.0 \pm 0.1$  mg<sub>s</sub> cm<sup>-2</sup> active mass loading and 0.5 g cm<sup>-3</sup> cathode density (80  $\mu\text{m}$ ). This results in slightly different cathode compositions for CNT BP (S:CNT = 50/50) and CNT DryFilm (S:CNT:PTFE = 50/47.5/2.5). The cathode discs are punched into circular discs of 15 mm diameter (1.767 cm<sup>2</sup>).

### Sulfur cathode preparation for pouch cells

The pouch cell development is carried out with three different CNT BP sheets (1.0, 1.5, and 2.0 mg<sub>BP</sub> cm<sup>-2</sup>). All electrodes are cut to the final pouch cell design (71  $\times$  46 mm<sup>2</sup>) for the lamination process onto a primer coated aluminum foil (20  $\mu\text{m}$ , MTI). The corresponding sulfur loading is adapted to  $50 \pm 1$  wt-%<sub>s</sub> sulfur by producing cathode loadings of 1.0, 1.5 and  $2.0 \pm 0.1$  mg<sub>s</sub> cm<sup>-2</sup>, respectively. Additionally, the combination of 2.0 mg<sub>BP</sub> cm<sup>-2</sup> CNT BP with  $1.0 \pm 0.1$  mg<sub>s</sub> cm<sup>-2</sup> sulfur is investigated to achieve  $33 \pm 1$  wt-%<sub>s</sub> sulfur content. Further investigations with perforated aluminum current collector are carried out with similar cathodes compositions. The foil receives circular perforation of 9.5 mm diameter. The lamination and infiltration process is kept constant.

### Electrochemical characterization

Coin cell assembly (CR2016) is carried out under argon atmosphere (MBraun, glove box, <0.01 ppm O<sub>2</sub> and H<sub>2</sub>O) and all cells are tested under same conditions at  $20^\circ\text{C} \pm 1\text{ K}$  by a cell test system (BaSyTec). The DME/DOL electrolyte system is mixed with 1 M LiTFSI (lithium bis(trifluoromethylsulfonyl)imide), 99.95%, anhydrous, BASF) and 0.25 M LiNO<sub>3</sub> (Lithium nitrate, 99.98%, anhydrous, Alfa Aesar) in DME (1,2-dimethoxy ethane, 99.5%, Sigma Aldrich) and DOL (1,3-dioxolane, 99.8%, Sigma Aldrich) (1:1, v/v). LiTFSI and LiNO<sub>3</sub> are dried at 120 °C in vacuum and all solvents are purified by threefold molecular sieve extraction (3 Å). Vacuum dried cathodes (1 h, 50 °C) with constant composition are assembled versus lithium metal chips (thickness: 250  $\mu\text{m}$ , diameter: 16.5 mm, purity: 99.9%, MTI Corp) and are separated by a polypropylene separator (diameter: 19 mm, thickness: 25  $\mu\text{m}$ , Celgard2500). The electrolyte volume is calculated for an electrolyte volume of 7.0  $\mu\text{L mg}_s^{-1}$  (25  $\mu\text{L} \sim 2.0$  mg<sub>s</sub> cm<sup>-2</sup>). The voltage window for DME/DOL is kept constant during all measurements (2.6 V–1.8 V). Galvanostatic discharge and charge currents are calculated by the specific capacity of sulfur (1672 mAh g<sub>s</sub><sup>-1</sup>). Long term measurements are tested at 0.1 C discharge rate (0.33 mA cm<sup>-2</sup>) and rate capability testing is carried out with different discharge rate between 0.1 C, 0.2 C, 0.5 C and 1 C. All measurements are preceded by a formation cycle 0 at 0.05 C. The charge rate is kept constant at 0.1 C. Cyclic voltammetry is carried out with 0.01 mV s<sup>-1</sup> scan rate between 2.6 V–1.8 V (BioLogic).

Pouch cell assembly is carried out under argon atmosphere (MBraun, glove box, <0.01 ppm O<sub>2</sub> and H<sub>2</sub>O) Three double-sided cathodes (Vacuum dried for 1 h at 50 °C) are prepared for the respective pouch cells. Lithium metal foil (thickness: 50  $\mu\text{m}$ , CEL China Energy Lithium Co., Ltd) and PE separator (thickness: 12  $\mu\text{m}$ ) are used for cell assembly and the electrolyte volume is set to

4  $\mu\text{L mg}^{-1}$  of DME/DOL. The cells with perforated aluminum current collector are filled with 4.5  $\mu\text{L mg}^{-1}$  electrolyte. Rate capability testing is carried out with different discharge C-rates between 0.1 C, 0.2 C, 0.5 C and 1 C (2.6 V–1.8 V). All measurements are preceded by a formation cycle 0 at 0.05 C and the charge rate is kept constant at 0.1 C. All currents are calculated by the specific capacity of sulfur (1672  $\text{mAh g}^{-1}$ ). The pouch cells are cycled under constant pressure by a hydraulic pressure control (Fraunhofer IWS). The calculation of specific energy ( $\text{Wh kg}^{-1}$ ) as a function of C-rate is based for all pouch cells on stack level for three double-sided cathodes and experimental electrolyte volume without any packaging and tabs.

## Acknowledgements

The research was financed by the German Ministry of Education and Research (BMBF) in the projects "HiPoLiS" (support code: 03XP0178 A) and by the European Social Fund ESF (Europäischer Sozialfonds) and the Free State of Saxony (Sächsische Aufbaubank – SAB) in the project "E-carbon" (Support code: 100310387). The authors acknowledge especially Kelly Henze (Fraunhofer IWS) for the sulfur cathode preparation. Many thanks for analytic measurements and cell assembly go to Sahin Cangaz, Christian Kensy, Sebastian Tschöcke, Peter Fleischer, Jeannette Strangalies and Susann Kleber (all Fraunhofer IWS), Dr. Ilka Kunert and Dr. Nelly Weiß (both TU Dresden). Open access funding enabled and organized by Projekt DEAL.

## Conflict of Interest

The authors declare no conflict of interest.

**Keywords:** lithium-sulfur battery • high power pouch cells • carbon nanotube cathodes • perforated current collector • sulfur transfer melt infiltration

- [1] M. Armand, J.-M. Tarascon, *Nature* **2008**, *451*, 652.
- [2] Mark Crittenden, "With Ultralight Lithium-Sulfur Batteries, Electric Airplanes Could Finally Take Off. Oxis Energy's design promises outstanding energy density, manufacturability, and safety", can be found under <https://spectrum.ieee.org/aerospace/aviation/with-ultra-light-lithium-sulfur-batteries-electric-airplanes-could-finally-take-off>, 2020.
- [3] A. Fotouhi, D. Auger, L. O'Neill, T. Cleaver, S. Walus, *Energies* **2017**, *10*, 1937.
- [4] T. Cleaver, P. Kovacik, M. Marinescu, T. Zhang, G. Offer, *J. Electrochem. Soc.* **2018**, *165*, A6029–A6033.
- [5] a) L. F. Nazar, M. Cuisinier, Q. Pang, *MRS Bull.* **2014**, *39*, 436; b) A. Varzi, K. Thanner, R. Scipioni, D. Di Lecce, J. Hassoun, S. Dörfler, H. Althues, S. Kaskel, C. Prehal, S. A. Freunberger, *J. Power Sources* **2020**, *480*, 228803.
- [6] G. Howells, "OXIS Energy is close to achieving 500 Wh/kg and is targeting 600 Wh/kg with Solid State Lithium Sulfur technology", can be found under <https://45uevg34gwltbsf2plyu1-wpengine.netdna-ssl.com/wp-content/uploads/2020/01/500-and-600-whkg-pressor.pdf>, 2020.
- [7] a) Q. Pang, X. Liang, A. Shyamsunder, L. F. Nazar, *Joule* **2017**, *1*, 871; b) D. Lin, Y. Liu, Y. Cui, *Nat. Nanotechnol.* **2017**, *12*, 194; c) M. Piwko, C. Weller, F. Hippauf, S. Dörfler, H. Althues, S. Kaskel, *J. Electrochem. Soc.* **2018**, *165*, A1084–A1091; d) D. Aurbach, E. Pollak, R. Elazari, G. Salitra, C. S. Kelley, J. Affinito, *J. Electrochem. Soc.* **2009**, *156*, A694.
- [8] X.-B. Cheng, J.-Q. Huang, Q. Zhang, *J. Electrochem. Soc.* **2018**, *165*, A6058–A6072.
- [9] a) J.-H. Cheng, A. A. Assegie, C.-J. Huang, M.-H. Lin, A. M. Tripathi, C.-C. Wang, M.-T. Tang, Y.-F. Song, W.-N. Su, B. J. Hwang, *J. Phys. Chem. C* **2017**, *121*, 7761; b) H. Yang, E. O. Fey, B. D. Trimm, N. Dimitrov, M. S. Whittingham, *J. Power Sources* **2014**, *272*, 900.
- [10] P. Bai, J. Li, F. R. Brushett, M. Z. Bazant, *Energy Environ. Sci.* **2016**, *9*, 3221.
- [11] S. Dörfler, S. Walus, J. Locke, A. Fotouhi, D. J. Auger, N. Shateri, T. Abendroth, P. Härtel, H. Althues, S. Kaskel, *Energy Technol.* **2020**.
- [12] C. Qu, Y. Chen, X. Yang, H. Zhang, X. Li, H. Zhang, *Nano Energy* **2017**, *39*, 262.
- [13] Lain, Brandon, Kendrick, *Batteries* **2019**, *5*, 64.
- [14] J. Zheng, D. Lv, M. Gu, C. Wang, J.-G. Zhang, J. Liu, J. Xiao, *J. Electrochem. Soc.* **2013**, *160*, A2288–A2292.
- [15] J. Brückner, S. Thieme, H. T. Grossmann, S. Dörfler, H. Althues, S. Kaskel, *J. Power Sources* **2014**, *268*, 82.
- [16] K. Takahashi, Y. Ishino, W. Murata, Y. Umebayashi, S. Tsuzuki, M. Watanabe, H. Takaba, S. Seki, *RSC Adv.* **2019**, *9*, 24922.
- [17] H. Nagata, Y. Chikusa, *J. Power Sources* **2014**, *264*, 206.
- [18] C.-W. Lee, Q. Pang, S. Ha, L. Cheng, S.-D. Han, K. R. Zavadil, K. G. Gallagher, L. F. Nazar, M. Balasubramanian, *ACS Cent. Sci.* **2017**, *3*, 605.
- [19] T. Zhang, M. Marinescu, S. Walus, P. Kovacik, G. J. Offer, *J. Electrochem. Soc.* **2018**, *165*, A6001–A6004.
- [20] D. Di Lecce, V. Marangon, W. Du, D. J. L. Brett, P. R. Shearing, J. Hassoun, *J. Power Sources* **2020**, *472*, 228424.
- [21] a) R. Fang, K. Chen, L. Yin, Z. Sun, F. Li, H.-M. Cheng, *Adv. Mater.* **2019**, *31*, e1800863; b) W. Zheng, Y. W. Liu, X. G. Hu, C. F. Zhang, *Electrochim. Acta* **2006**, *51*, 1330; c) X. Ji, K. T. Lee, L. F. Nazar, *Nat. Mater.* **2009**, *8*, 500; d) R. Elazari, G. Salitra, A. Garsuch, A. Panchenko, D. Aurbach, *Adv. Mater.* **2011**, *23*, 5641; e) J.-Y. Song, H.-H. Lee, W. G. Hong, Y. S. Huh, Y. S. Lee, H. J. Kim, Y.-S. Jun, *Nanomaterials* **2018**, *8*.
- [22] R. Fang, G. Li, S. Zhao, L. Yin, K. Du, P. Hou, S. Wang, H.-M. Cheng, C. Liu, F. Li, *Nano Energy* **2017**, *42*, 205.
- [23] a) S. Dörfler, P. Strubel, T. Jaumann, E. Troschke, F. Hippauf, C. Kensy, A. Schökel, H. Althues, L. Giebel, S. Oswald et al., *Nano Energy* **2018**, *54*, 116; b) T.-Z. Hou, X. Chen, H.-J. Peng, J.-Q. Huang, B.-Q. Li, Q. Zhang, B. Li, *Small* **2016**, *12*, 3283; c) H. Tang, W. Li, L. Pan, C. P. Cullen, Y. Liu, A. Pakdel, D. Long, J. Yang, N. McEvoy, G. S. Duesberg et al., *Adv. Sci.* **2018**, *5*, 1800502.
- [24] C. Kensy, P. Härtel, J. Maschita, S. Dörfler, B. Schumm, T. Abendroth, H. Althues, B. V. Lotsch, S. Kaskel, *Carbon* **2020**, *161*, 190.
- [25] S. Risse, C. J. Jafta, Y. Yang, N. Kardjilov, A. Hilger, I. Manke, M. Ballauff, *Phys. Chem. Chem. Phys.* **2016**, *18*, 10630.
- [26] S. Risse, E. Härt, B. Kent, M. Ballauff, *ACS Nano* **2019**, *13*, 10233.
- [27] R. Vajtai, *Springer Handbook of Nanomaterials*, Springer Berlin Heidelberg, Berlin, Heidelberg, 2013.
- [28] A. G. Rinzler, J. Liu, P. Nikolaev, C. B. Huffman, F. J. Rodríguez-Macías, P. J. Boul, A. H. Lu, D. T. Colbert, R. S. Lee, J. E. Fischer et al., *Appl. Phys. 1998*, *67*, 29.
- [29] a) Y.-S. Su, A. Manthiram, *Chem. Commun.* **2012**, *48*, 8817; b) Y. Fu, Y.-S. Su, A. Manthiram, *Angew. Chem.* **2013**, *52*, 6930; c) S.-H. Chung, C.-H. Chang, A. Manthiram, *Small* **2016**, *12*, 939; d) C. Zhang, L. Cui, S. Abdolhosseiniزاده, J. Heier, *InfoMat* **2020**, *2*, 613; e) H. Tang, W. Li, L. Pan, K. Tu, F. Du, T. Qiu, J. Yang, C. P. Cullen, N. McEvoy, C. Zhang, *Adv. Funct. Mater.* **2019**, *29*, 1901907.
- [30] Z. Yuan, H.-J. Peng, J.-Q. Huang, X.-Y. Liu, D.-W. Wang, X.-B. Cheng, Q. Zhang, *Adv. Funct. Mater.* **2014**, *24*, 6105.
- [31] S. Dörfler, M. Hagen, H. Althues, J. Tübke, S. Kaskel, M. J. Hoffmann, *Chem. Commun.* **2012**, *48*, 4097.
- [32] S. Thieme, J. Brückner, I. Bauer, M. Oschatz, L. Borchardt, H. Althues, S. Kaskel, *J. Mater. Chem. A* **2013**, *1*, 9225.
- [33] a) S.-H. Chung, K.-Y. Lai, A. Manthiram, *Adv. Mater.* **2018**, *30*, e1805571; b) R. Carter, L. Oakes, N. Muralidharan, C. L. Pint, *J. Phys. Chem. C* **2017**, *121*, 7718; c) M. Zheng, Y. Chi, Q. Hu, H. Tang, X. Jiang, L. Zhang, S. Zhang, H. Pang, Q. Xu, *J. Mater. Chem. A* **2019**, *7*, 17204; d) L. Qie, A. Manthiram, *ACS Energy Lett.* **2016**, *1*, 46; e) C. Dillard, S.-H. Chung, A. Singh, A. Manthiram, V. Kalra, *Mater. Today* **2018**, *9*, 336; f) M. Li, R. Carter, A. Douglas, L. Oakes, C. L. Pint, *ACS Nano* **2017**, *11*, 4877.
- [34] a) D. Yadav, F. Amini, A. Ehrmann, *Eur. Polym. J.* **2020**, *138*, 109963; b) M. Kumar, Y. Ando, *J. Nanosci. Nanotechnol.* **2010**, *10*, 3739.
- [35] M. Kumar, Y. Ando, *J. Nanosci. Nanotechnol.* **2010**, *10*, 3739.

- [36] M. Endo, K. Takeuchi, K. Kobori, K. Takahashi, H. W. Kroto, A. Sarkar, *Carbon* **1995**, *33*, 873.
- [37] O. V. Kharissova, B. I. Kharisov, *RSC Adv.* **2014**, *4*, 30807.
- [38] a) C. Thomsen, S. Reich, Light Scattering in Solid IX **108**, 115; b) A. Nish, J.-Y. Hwang, J. Doig, R. J. Nicholas, *Nat. Nanotechnol.* **2007**, *2*, 640.
- [39] M. S. Dresselhaus, G. Dresselhaus, R. Saito, A. Jorio, *Phys. Rep.* **2005**, *409*, 47.
- [40] M. S. Dresselhaus, A. Jorio, A. G. Souza Filho, R. Saito, *Phil. Trans. R. Soc. A* **2010**, *368*, 5355.
- [41] S. Dörfler, I. Felhösi, T. Marek, S. Thieme, H. Althues, L. Nyikos, S. Kaskel, *J. Power Sources* **2013**, *227*, 218.
- [42] a) X.-W. Lei, Q.-Q. Ni, J.-X. Shi, T. Natsuki, *Nano Res.* **2011**, *6*, 492; b) X. Zhao, Y. Ando, L.-C. Qin, H. Kataura, Y. Maniwa, R. Saito, *Chem. Phys. Lett.* **2002**, *361*, 169.
- [43] a) R. Saito, H. Kataura, Synthetic metals **80**, 213; b) Costa, Borowiak-Palen, Kruszynska, *Materials Science-Poland* **2008**.
- [44] M. G. Donato, S. Galvagno, M. Lanza, G. Messina, C. Milone, E. Piperopoulos, A. Pistone, S. Santangelo, *J. Nanosci. Nanotechnol.* **2009**, *9*, 3815.
- [45] D. Mishra, R. Arora, S. Lahiri, S. S. Amritphale, N. Chandra, *Prot Met Phys Chem Surf* **2014**, *50*, 628.
- [46] a) M. Hijiri, *J. Mater. Sci. Mater. Electron.* **2020**, *31*, 5025; b) A. Ali, M. S. AlSalhi, M. Atif, A. A. Ansari, M. Q. Israr, J. R. Sadaf, E. Ahmed, O. Nur, M. Willander, *J. Phys. Conf. Ser.* **2013**, *414*, 12024.
- [47] R. Y. Chen, *Oxid. Met.* **2003**, *59*, 433.
- [48] K. Y. Tran, B. Heinrichs, J.-F. Colomer, J.-P. Pirard, S. Lambert, *Appl. Catal. A* **2007**, *318*, 63.
- [49] A. Yahyazadeh, B. Khoshandam, *Results Phys.* **2017**, *7*, 3826.
- [50] a) N. Tripathi, P. Mishra, B. Joshi, Harsh, S. S. Islam, *Physical E* **2020**; b) L. He, S. Hu, L. Jiang, G. Liao, X. Chen, H. Han, L. Xiao, Q. Ren, Y. Wang, S. Su et al., *Fuel Process. Technol.* **2018**, *176*, 7; c) S. Shukrullah, M. Y. Naz, N. M. Mohamed, K. A. Ibrahim, A. Ghaffar, N. M. AbdEl-Salam, *J. Nanomater.* **2019**, *2019*, 1.
- [51] M. A. Nguyen, D. T. Ngo, T. van Le, D. V. Cao, *Adv. Nat. Sci. Nanosci. Nanotechnol.* **2013**, *4*, 35018.
- [52] M. Thommes, K. Kaneko, A. V. Neimark, J. P. Olivier, F. Rodriguez-Reinoso, J. Rouquerol, K. S. W. Sing, *Pure Appl. Chem.* **2015**, *87*, 1051.
- [53] S. Dörfler, I. Felhösi, I. Kék, T. Marek, H. Althues, S. Kaskel, L. Nyikos, *J. Power Sources* **2012**, *208*, 426.
- [54] a) Y. V. Mikhaylik, J. R. Akridge, *J. Electrochem. Soc.* **2004**, *151*, A1969; b) S. S. Zhang, *Electrochim. Acta* **2012**, *70*, 344.
- [55] M. Zhao, B.-Q. Li, H.-J. Peng, H. Yuan, J.-Y. Wei, J.-Q. Huang, *Angew. Chem.* **2019**.
- [56] M. Wild, G. J. Offer (Eds.) *Lithium-Sulfur Batteries*, John Wiley & Sons, Ltd, Chichester, UK, 2019.
- [57] Y. Wei, Y. Tao, C. Zhang, J. Wang, W. Qiao, L. Ling, D. Long, *Electrochim. Acta* **2016**, *188*, 385.
- [58] X. Huang, Z. Wang, R. Knibbe, B. Luo, S. A. Ahad, D. Sun, L. Wang, *Energy Technol.* **2019**, *7*, 14.
- [59] S. Dörfler, H. Althues, P. Härtel, T. Abendroth, B. Schumm, S. Kaskel, *Joule* **2020**, *4*, 539.
- [60] M. Wild, L. O'Neill, T. Zhang, R. Purkayastha, G. Minton, M. Marinescu, G. J. Offer, *Energy Environ. Sci.* **2015**, *8*, 3477.
- [61] a) T. Zhang, M. Marinescu, L. O'Neill, M. Wild, G. Offer, *Phys. Chem. Chem. Phys.* **2015**, *17*, 22581; b) S. Drvarič Talian, G. Kapun, J. Moškon, A. Vizintin, A. Randon-Vitanova, R. Dominko, M. Gaberšček, *Chem. Mater.* **2019**, *31*, 9012.

Manuscript received: February 2, 2021

Revised manuscript received: March 3, 2021

Accepted manuscript online: March 15, 2021

Version of record online: March 18, 2021